Authors' accepted manuscript.
Mechanism and Machine Theory, 2015
The final publication is available at:
http://dx.doi.org/10.1016/j.mechmachtheory.2015.04.018

Design and analysis of a flexible linkage for robot safe operation in collaborative scenarios

Javier López-Martínez[a,*], José Luis Blanco-Claraco[a], Daniel García-Vallejo[b], Antonio Giménez-Fernández[a]

[a] *Department of Engineering, University of Almería, Spain*
[b] *Department of Mechanical Engineering and Manufacturing, University of Seville, Spain*

Abstract

One of the most serious security issues for collaborative work between robots and humans is the potential damage caused by unexpected collisions between them. Intrinsically-safe systems are a must in order to assure safety for both, the user and the robot, under the worst-case scenario of a total failure of the control subsystem. This work contributes to the field of passive mechanical system safety. The proposed security system consists in a flexible linkage that splits a robot arm link in two parts. Such a linkage allows the link to remain completely rigid as long as a given torque threshold is not exceeded, with that threshold being configurable according to working conditions and safety considerations. Both theoretical and experimental tests demonstrate a significant reduction in the accelerations and forces generated by impacts between the end effector of a robot arm equipped with the proposed mechanism and a simplified human head model.

Keywords: Flexible linkages, safety systems, robot arm

1. Introduction

New security systems are required in the design of robots for applications where they share their workspace with humans, with the subsequent risk of accidental collisions, if we are to guarantee the safety of humans and the integrity of machines [1]. The search for intrinsically-safe robot mechanical designs has been already addressed in the literature,

*Corresponding author
Email addresses: javier.lopez@ual.es (Javier López-Martínez), jlblanco@ual.es (José Luis Blanco-Claraco), dgvallejo@us.es (Daniel García-Vallejo), agimfer@ual.es (Antonio Giménez-Fernández)

focusing fundamentally on the combination of reducing the inertia of robot arms and the addition of flexible components to their structure.

Passive mechanical systems proposed so far exploit the structural flexibility of links [2], joint flexibility [3, 4] and soft coverings [5, 6, 7]. Among them, the latter approach has demonstrated the best results in reducing impact forces and induced accelerations in the case of an collision between a robot arm and a human head [2]. Joint flexibility, by means of decoupling rotor inertia from the end link inertia, also contributes an safety improvement in the event of an impact. In this sense, there has been interest in Variable Stiffess Actuators (VSAs) [3, 8, 9] as decoupling mechanisms. However, Haddadin *et al.* [10] showed that the reduced joint stiffness of robot DLR-LWRIII (mainly due to Harmonic Drive gears) is enough to decouple motor inertia from link inertia, hence any further increase in joint flexibility will not attenuate impact forces during a blunt impact. These results were later confirmed through simulations [2] where, for an ideally rigid link, an ordinary gear transmission was enough to decouple rotor inertia. Finally, the internal flexibility of the robot links also has its own positive effects in damage reduction, although in this case a trade-off must be achieved since excessive flexibility hardens the positioning control of the robot end effector [11].

A robotic manipulator with the potential of working closely with humans should be able, ideally, to operate with a reduced stiffness whenever it exists any risk of collision (hence, dangerous high forces), while also being able of exhibiting high stiffness in other operations. Following this idea, researchers have proposed VSAs and some flexible mechanisms for robot joints with nonlinear stiffness characteristics. The latter have decreasing stiffness curves, that is, the joint features high stiffness for reduced deformations but quickly decreases after the force reach some predefined threshold [4, 12]. In this respect, Park *et al.* proposed in [13] a safe link mechanism based on a flexible mechanism amid a robot link. This device includes a double slider mechanism and a spring attached to one of them, such that for a given initial configuration one attains the desired effect of nonlinear stiffness depending on deformation.

Following this concept of introducing a flexible element amid the link instead of at a joint, the present work presents a novel flexible linkage aimed at operation safety. The proposed flexible linkage is located in the middle of a robot link, splitting the link in two, and therefore decoupling the inertia at each side in the event of an impact. The two links remain coupled by means of a mechanism comprising a spring, a cable and a tensor element as will be discussed below. Its main characteristic is the ability to sustain the maximum structural stiffness of the rigid link as long as the external load does not exceed a given threshold value, quickly reducing the stiffness otherwise. In comparison to previous proposals this new flexible linkage features a very simple construction and the ability to easily vary the threshold after which the flexibility of the linkage acts.

The rest of this work is structured as follows. Section 2 firstly introduces the conceptual design, some implementations solutions and the kinematic model. Next, Section 3 presents a mathematical model of the impact between the end effector of a robot arm, including a flexible linkage, and a dummy human head; and analyzes the contribution to safety due to the linkage. Section 4 describes the mechanical implementation of the prototype linkage, the experimental setup devised to assess the performance of the proposed flexible linkage in the context of a robot arm-human head collision, and experimental results. Finally, we conclude with a discussion of the obtained results.

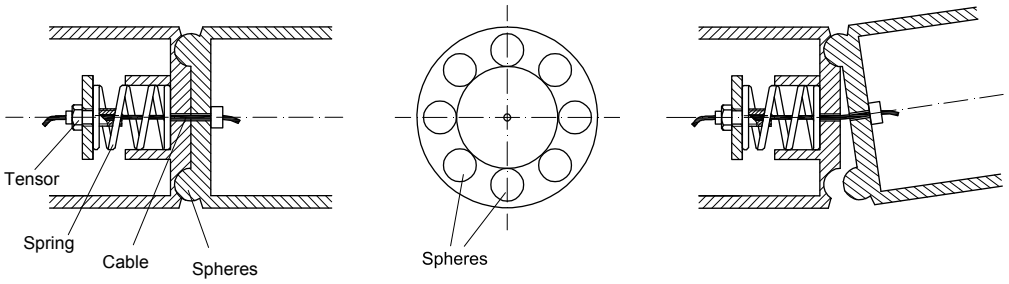

Figure 1: Sketch of the flexible link, (a)–(b) in its rest configuration and (c) under an external load that forces it to rotate.

2. Proposed mechanism

In the following we describe the basis of the proposed security flexible linkage, along with a mathematical modeling of its stiffness curve as a function of the angular rotation of the linkage.

2.1. Conceptual design

The linkage comprises two rigid bases placed face to face, perfectly coupled to each other by means of a circular array of equally spaced pockets and spherical protuberances, as illustrated in Figure 1. Such sphere layout allows the relative rotation of the two bases around an axis contained in the plane described by the center(s) of the sphere(s). The relative rotation may happen either having only one sphere in contact with its corresponding pocket or having two consecutive spheres in contact with their pair pocket. Depending on the number of spheres in contact with pockets, the axis of rotation will be passing through the center of two consecutive spheres or only passing through one. A compression helical spring is supported by the inner face of one of the two base parts, and compressed by a tensor and a steel cable in order to maintain the two parts of the mechanism in contact. As will be discussed below, the external load required to induce the rotation of the two bases depends on the spring preload at rest.

Together with its construction simplicity, the main novelty of the proposed mechanism is the capability of easily changing the load level at which the flexible linkage begins to act, with the particularity of having the same stiffness right after that point regardless of the selected load threshold. Therefore, the arm behaves as if it was a rigid link as long as the load threshold is not exceeded.

Two possible designs of how to dynamically vary the preload of the proposed flexible linkage are shown in Figure 2. However, it must be noted that the introduction of a tunable preload carries the cost of having to include an electric motor and a transmission system, increasing the overall mass of the system. Figure 2(a) shows the first design, including a worm gear screw where the cable of the tensor mechanism rolls over the gear shaft. A different solution is shown in Figure 2(b) were the motor shaft directly drives the tensor screw.

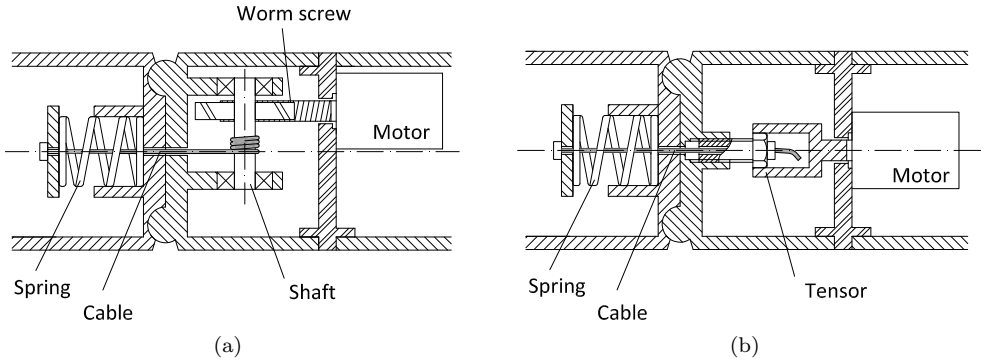

Figure 2: Two possible implementations of varying, actuated preload in the proposed flexible linkage: (a) based on a worm gear screw and (b) with a tensor screw.

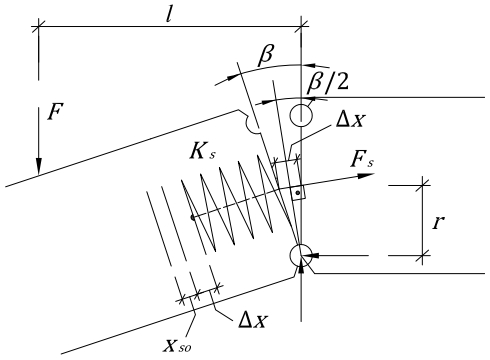

Figure 3: Sketch of the linkage under an external force, illustrating the meaning of all the variables involved in its characterization.

2.2. Analysis of the linkage stiffness

We now address the derivation of a closed-form, theoretical expression for the kinematic behavior of the proposed flexible linkage. In the following, please refer to Figure 3 for an illustration of the physical meaning of each variable.

The initial preload of the spring, F_{si}, is given by its stiffness K_s and its initial compression x_{so}, such that:

$$F_{si} = K_s x_{so}. \tag{1}$$

Rotation of the linkage can only occur by means of pivoting at the spheres, placed at a distance r from the linkage axis of symmetry, where the tension of the cable also acts. Therefore, the torque required to separate the two parts of the linkage is given by:

$$T_i = r F_{si}. \tag{2}$$

Here the distance of rotation r has been assumed constant. This distance will vary slightly depending on the direction of rotation: the shortest achievable distance of rotation is found along the perpendicular between the linkage axis of symmetry and a line

crossing the centers of two neighboring spheres, while the largest distance of rotation is the previously described distance r. Hence, a high number of spheres is desirable to minimize as much as possible these small distance variations. Once the torque threshold given by Eq.(2) is surpassed, we find a variable stiffness depending on the rotation β between the two parts of the mechanism. As can be seen from the geometry of the problem, in Figure 3, the spring compression Δx is related to the rotation by:

$$\Delta x = 2r \sin \frac{\beta}{2}. \tag{3}$$

Invoking the equations of static equilibrium, and using Eqs.(1) and (3), the cable tension F_s becomes:

$$F_s = K_s \left(x_{so} + \Delta x\right) = F_{si} + 2K_s r \sin \frac{\beta}{2}. \tag{4}$$

The total external torque (T) applied to one part of the mechanism under equilibrium can be obtained by summing all torques, e.g. with respect to the pivoting point, leading to:

$$\begin{aligned} T = Fl &= F_s r \cos \frac{\beta}{2} \\ &= F_{si} r \cos \frac{\beta}{2} + K_s r^2 \sin \beta. \end{aligned} \tag{5}$$

Finally, we arrive at the expression of the stiffness (K_l) by taking derivatives of Eq.(5) with respect to rotation β:

$$\begin{aligned} K_l &= \frac{dT}{d\beta} \\ &= -\frac{1}{2} F_{si} r \sin \frac{\beta}{2} + K_s r^2 \cos \beta, \quad \text{for } T > T_i. \end{aligned} \tag{6}$$

The first term in Eq. (6), which depends on the initial preload of the spring, is negligible in practice for small deformations due to the $\sin \beta/2$ term. The second term thus dominates the theoretical stiffness for small deformations, introducing a dependency on the spring stiffness, K_s, and the linkage radius of rotation, r. Therefore, it follows our claim of the proposed mechanism exhibiting a small-deformation stiffness which is independent of initial preloading and, subsequently, of the desired torque threshold, T_i.

3. Impact model and safety contribution

The contribution of the proposed flexible linkage on injury reduction is studied through a mathematical model of the impact between the end effector of a robot arm incorporating the linkage and a human head.

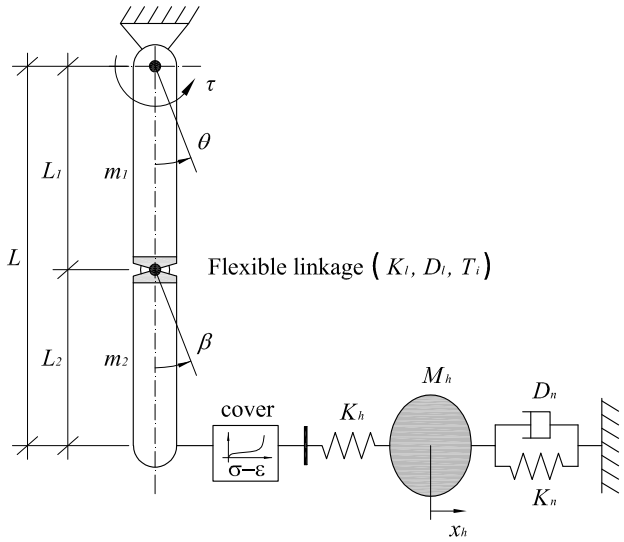

Figure 4: Impact model between the end effector of a robot arm with flexible linkage and a human head-neck complex.

3.1. Robot arm-human head impact model

The planar model of Figure 4 represents a single-link manipulator with a flexible linkage. The arm, with an overall length L, is divided thought the linkage in the proximal link, L_1, and the distal link, L_2. Both segments of the robot arm are approximated as rigid bodies. The impact with the human head takes place at the final end of the distal link, where the contact includes a phenomenological model of a polyurethane foam used as soft cover, and the stiffness of the skull represented as a linear spring of $2.0 \cdot 10^6$ N/m stiffness constant (K_h) [14], both elements arranged in series. The human head-neck system can be simplified to a 1 d.o.f. model with mass M_h and a spring with stiffness constant K_n in parallel with a damper with damping coefficient D_n. Values of stiffness and damping coefficient for a rotational 1 d.o.f. model of the head-neck complex have been identified in several studies [15, 16, 17]. In this work, an equivalent system consisting of a single translational d.o.f. is used with a stiffness coefficient of 463 N/m, a damping coefficient of 20.8 Ns/m and a human head-neck mass of 3.25 kg are assumed [2].

The equations of motion for the robot-human head impact model of Figure 4 are obtained as follows:

$$\mathbf{M}\ddot{\mathbf{q}} + \mathbf{D}\dot{\mathbf{q}} + \mathbf{K}\mathbf{q} \quad = \quad \mathbf{Q}_e + \mathbf{Q}_c + \mathbf{Q}_v \tag{7}$$

In Eq.(7), $\mathbf{q}$ denotes the vector of system independent coordinates, $\mathbf{M}$ is the system mass matrix, $\mathbf{D}$ is the damping matrix, $\mathbf{K}$ is the stiffness matrix, $\mathbf{Q}_e$ is the vector of generalized externally applied forces, $\mathbf{Q}_c$ is the vector of generalized nonlinear contact forces and $\mathbf{Q}_v$ is the vector of generalized centrifugal and Coriolis inertia forces. Eq.(7) can be written in matrix form as

$$\begin{bmatrix} m_{11} & m_{12} & 0 \\ m_{21} & m_{22} & 0 \\ 0 & 0 & M_h \end{bmatrix} \begin{bmatrix} \ddot{\theta} \\ \ddot{\beta} \\ \ddot{x}_h \end{bmatrix} + \begin{bmatrix} 0 & 0 & 0 \\ 0 & D_l & 0 \\ 0 & 0 & D_n \end{bmatrix} \begin{bmatrix} \dot{\theta} \\ \dot{\beta} \\ \dot{x}_h \end{bmatrix} + \begin{bmatrix} 0 & 0 & 0 \\ 0 & K_l & 0 \\ 0 & 0 & K_n \end{bmatrix} \begin{bmatrix} \theta \\ \beta \\ x_h \end{bmatrix} =$$
$$\begin{bmatrix} (Q_e)_\theta \\ (Q_e)_\beta \\ (Q_e)_{x_h} \end{bmatrix} + \begin{bmatrix} (Q_c)_\theta \\ (Q_c)_\beta \\ (Q_c)_{x_h} \end{bmatrix} + \begin{bmatrix} (Q_v)_\theta \\ (Q_v)_\beta \\ 0 \end{bmatrix} \tag{8}$$

The vector $\mathbf{Q}_e$ of external forces includes gravity and the actuator torque, τ. Coordinates $\mathbf{q}$ comprise the angular position of the arm, θ, the angular deviation of the linkage, β, and the head displacement, x_h (see Figure 4). The terms m_{11} and m_{12} of the symmetric mass matrix $\mathbf{M}$ depend on the mass, length, and relative position of both links (β), while the term m_{22} is constant and equal to the inertia of the distal link. Damping and stiffness matrices are symmetric positive semi-definite. The damping matrix $\mathbf{D}$ includes all damping effects of the linkage and the neck. The stiffness matrix $\mathbf{K}$ includes restoring forces due to neck flexibility as well as the stiffness curve of the linkage, where the linkage can be assumed ideally rigid, or with a very high stiffness, while the torque reflected at the linkage remains below the torque threshold T_i. Figure 5 graphically represents the torque (T) and stiffness (K_l) curves for different rotation angles (β) between the two parts of the mechanism and for different preload values (x_{so}) of the compression spring. These curves have been obtained based on Eqs. (5)–(6), where values of spring stiffness constant $K_s = 44.0$ kN/m and rotation distance $r = 28$ mm are used. As can be seen in Figure 5(a), and from Eq.(1) and Eq.(2), the torque threshold to start separating the two parts of the mechanism is proportional to the preload values. Once the threshold is surpassed, the initial stiffness is the same disregarding the preload value, as can be seen in Figure 5(b). Different preload values lead to minor differences in how the non-linear stiffness changes with the rotation angle, where for large rotation angles differences on linkage stiffness become important. It must be noted that in the experiments performed during this research work maximum rotations at impacts will be around 15^o, then, only the first interval of small angles will be of interest for practical applications.

It must be noted that equations in Section 2 must be corrected in order to consider the effect of the centrifugal force in the torque threshold value. The centrifugal force tends to separate the two parallel faces of the linkage increasing the load of the spring and decreasing the normal contact forces at the pocket-sphere pair. If the normal contact force at the pocket-sphere pair vanishes, spheres would separate leading to a critical configuration. Centrifugal force also exerts some effects on the torque threshold, as discussed next. The centrifugal force acts in an opposite direction to the spring force, so that the force F_{si} in Eqs.(2)–(6) where should be replaced by $F_{si} - F_c$, where F_c stands for the centrifugal force acting on the distal link. This implies a small reduction on the torque threshold when the robot arm moves at a high speed, which turns out to be a benefit on the side of safety.

The contact between the distal link and the human head is modeled by an elastic method in which the force between the link and the head is evaluated at any time based on the relative penetration. Then, the force is added into the equations of motion in vector $\mathbf{Q}_c$. During contact, the stiffness of the skull, K_h, has been considered to be in series with the compressive characteristics (stress-strain curve) of a robot arm cover of

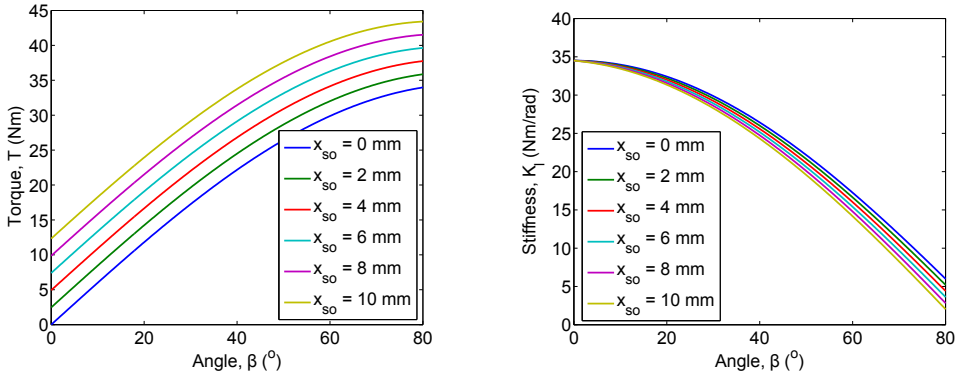

(a) (b)

Figure 5: For different initial compression (x_{so}) values, the graphs show theoretical predictions for (a) torque and (b) stiffness vs. linkage rotation angle.

polyurethane foam.

Compressive behavior of low weight cellular materials can be properly described through constitutive models [18, 19, 20]. In this work, the relationship between compressive stress and strain of a specimen of polyurethane foam has been measured experimentally in a compressive test. Then, a constitutive model has been fitted to experimental data. This model is used to compute the external forces included in Eq.(8).

Figure 6 depicts the stress-strain curves of a polyurethane foam specimen with density of 99 kg/m^3 and 12 mm thickness for different strain rates obtained in compressive tests performed on a servo-hydraulic test machine that includes a 5 kN axial actuator, showing that strain rates over 1.0 s^{-1} has minor influence in the resultant curve. Since the strain rate at impacts is higher than the maximum admissible compression rate accomplished by the test machine, it has been used the curve with the higher strain rate of 1.0 s^{-1}. The compression phase of this curve has been fitted by the Avalle *et al.* [20] model, described as:

$$\sigma = A\left(1 - e^{-\frac{E}{A}\epsilon(1-\epsilon)^m}\right) + B\left(\frac{\epsilon}{1-\epsilon}\right)^n \tag{9}$$

where σ and ϵ are engineering stress and engineering strain, and the five parameters A, E, m, B, n, are empirically determined. The parameters of the Avalle *et al.* model were obtained by least square fitting the experimental data (Table 1). Figure 7 shows a comparison between the experimental compression curve and the fitted curve, where a very good approximation is obtained. In this work, the curve fitted to the foam compression phase has been used to simulate the complete impact period, i.e. compression and decompression phase of the foam, which only slightly modifies the results obtained with a complete mathematical model including both curves [2]. In particular, the differences in time response curves only appear after the first peak force, slightly modifying the computed HIC_{36} value but not affecting the maximum force value.

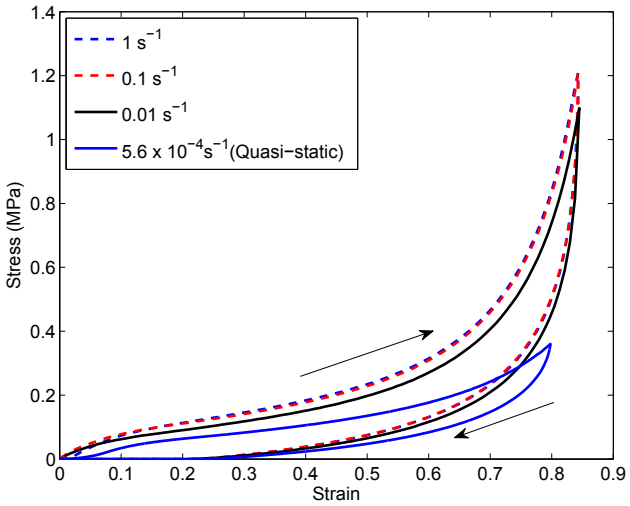

Figure 6: Stress-strain relation of the polyurethane foam specimen at different strain rates.

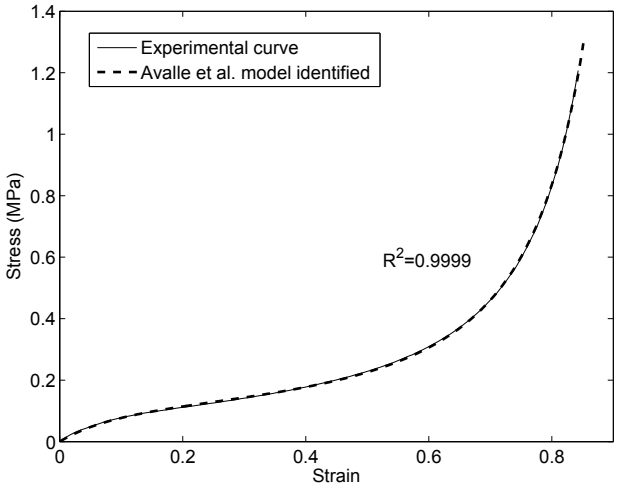

Figure 7: Comparison between the compression part of the experimental stress-strain curve and the curve predicted by the Avalle *et al.* [20] model.

Table 1: Avalle *et al.* [20] model parameters calculated from stress-strain compression curve fitting.

A (MPa)	B (MPa)	E (MPa)	m	n
0.1327	0.1239	1.186	1.612	1.328

Table 2: Parameters of the reference robot arm and human head-neck model.

Property	Value
Mass (kg)	$m_1 = m_2 = 3.0, M_h = 3.25$
Length (m)	$L = 0.7, L_1 = L_2 = 0.35$
Stiffness (N/m)	$K_n = 463, K_h = 2.0^6, K_l$ (from Eq. (6))
Damping (Ns/m)	$D_n = 20.8, D_l = 1.0$

3.2. Analysis of the flexible linkage's contribution to safety

The mathematical model introduced above is now used to evaluate the contribution of the flexible linkage to head injury reduction during a collision. In absence of specific head injury criteria for human robot impacts, most previous works have adopted the Head Injury Criteria (HIC) [21] and peak forces for head bone fracture [22] as severity indexes. Values of HIC_{36} of 10 and 100 have been used for several authors as a limit to assure human safety [8, 23, 13]. In this work, these limits are only used as reference, note that the aim of the following simulations is mainly to analyze the effect of the flexible linkage in the injury measures reduction regardless of its quantitative values.

Initially, a robot arm of 0.7 m length and a distributed mass of 6 kg has been used in simulations (Table 2). Flexible linkage is placed at the middle of the robot arm, hence, proximal and distal links are of equal length. It is assumed that the arm is moving at constant speed in a horizontal plane, with an impact speed of 2 m/s while no torque is exerted by the actuator (i.e. $\mathbf{Q}_e$ is null). All figures containing simulation results shown in this section start at the time of the initial contact between the head and the robot distal link, with the flexible linkage being undeformed when both bodies initially get into contact. The flexible linkage stiffness curve of Eq.(6) included in the mathematical model is computed for a spring stiffness constant $K_s = 44.0$ kN/m, a value of r of 28 mm, and for different initial compressions x_{so}. For torques below the linkage torque threshold, a linkage stiffness of $7.4 \cdot 10^4$ Nm/rad has been assumed, a high stiffness that attempts to take into account the arm and linkage internal flexibility for the sake of a more realistic model.

Figures 8–9 present a comparison of head accelerations and contact forces at impact, respectively, for different initial compressions (x_{so}) of the flexible linkage when a foam cover of 4 cm^2 contact area and 10 mm thickness is simulated. Time curves show two consecutive impacts, with the second impact getting closer in time to the first one as initial compression increases. For large values of x_{so} the two impacts overlaps and the first peak value increases. Higher initial compressions tend to have a similar behavior to a rigid link. In the figures, dashed black lines represent the resultant acceleration and contact force for a rigid robot arm without flexible linkage. Table 3 resumes the peak values for acceleration, contact force and HIC_{36} for each value of initial compression. Incorporating a flexible linkage leads to a peak force reduction of 40% and even greater HIC_{36} values reduction of 75%.

Figure 10 shows the contact force when no soft cover is used, i.e. only the stiffness of the skull is present. In this case, although two consecutive impacts are still present, the peak force of the first impact is almost the same as for a rigid link. To analyze the contribution on injury reduction of the flexible linkage with respect to cover stiffness, different polyurethane foam thicknesses have been simulated. As in the previous analy-

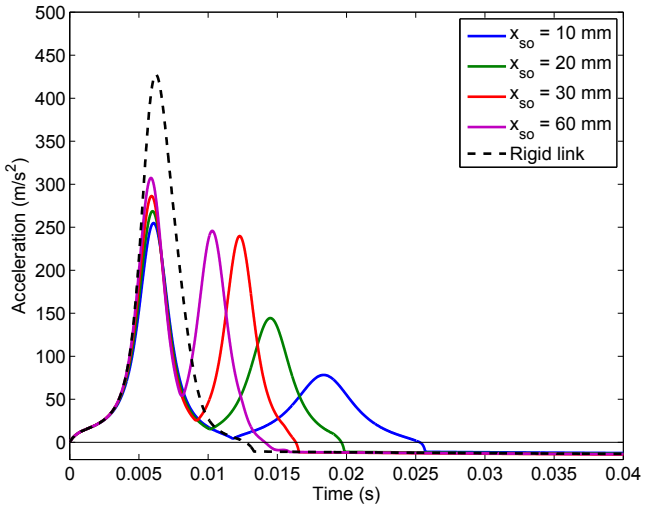

Figure 8: Head acceleration for different flexible linkage initial compression x_{so} and rigid link. Robot arm has soft cover.

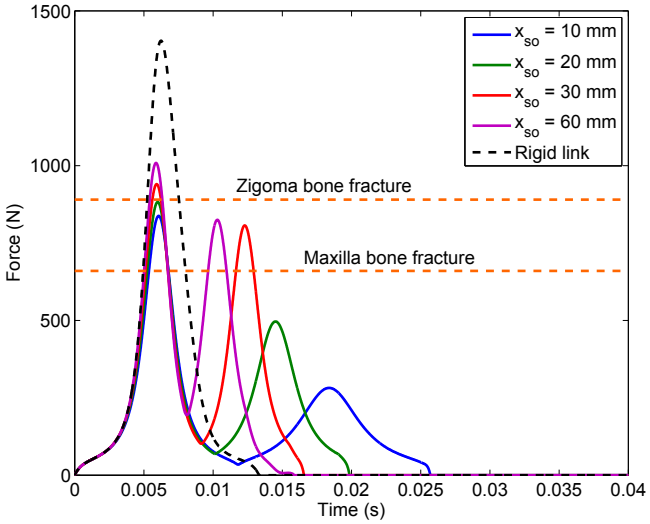

Figure 9: Contact force for different flexible linkage initial compression x_{so} and rigid link. Robot arm has soft cover.

Table 3: Peak force, peak acceleration and HIC_{36} for different linkage initial compression x_{so} and rigid link.

Linkage compression, x_{so} (mm)	10	20	30	60	rigid
Peak force (N)	838	882	940	1009	1404
Peak acceleration (m/s^2)	254	267	286	307	427
HIC_{36}	4.98	5.51	7.32	9.81	20.81

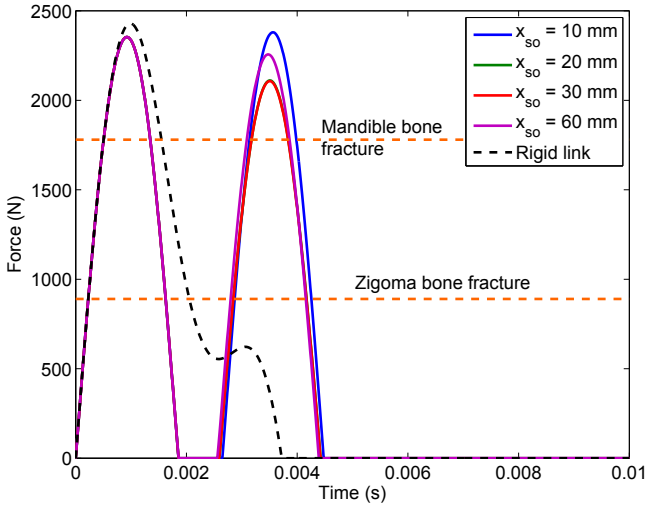

Figure 10: Contact force for different flexible linkage initial compression x_{so} and rigid link. Robot arm without soft cover.

ses, the phenomenological model of Avalle *et al.* has been employed, assuming that the stress-strain curve of the foam is the same regardless of the foam thickness. As a consequence, since cover stiffness is inversely proportional to its thickness, thicker foams lead to softer coverings. Figure 11 shows the peak contact force reduction with respect to the corresponding rigid arm for different initial compression of the linkage and for different cover thickness. For any initial compression curve there exists a cover thickness, between 15 mm and 20 mm, that maximizes the force reduction with respect to a rigid arm. As predicted from Figure 10, reduction of cover thickness, i.e. more rigid impacts, leads to contact forces similar to those of completely rigid arms, minimizing the benefits of the flexible linkage. Cover thicknesses over a value of approximately 20 mm also lead to a reduction of the linkage effects, but in a more progressive way. Furthermore, for high initial compressions as x_{so}=60 mm, the obtained torque does not overcome the linkage threshold when foam cover has a thickness equal or greater than 45 mm (see Figure 11).

Changes in robot model parameters will also have effects in the resultant force reduction and in the interval of cover thicknesses where the linkage properly works. Figure 12 represents the results for different placements of the linkage along the robot arm and, as one could expect, shorter distal links result in further force reductions. In addition, Figure 13 shows variations in the overall robot arm mass, where the region of maximum

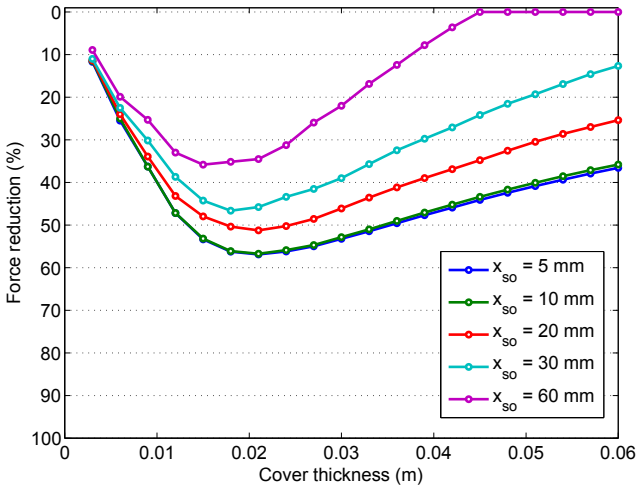

Figure 11: Peak contact force reduction (with respect to the rigid link) vs. cover thickness for different linkage initial compression x_{so}.

force reduction moves towards higher thicknesses as robot mass increases.

Since incorporating a flexible linkage might compromise the usability of the robot, its design parameters should be selected such that the robot arm is kept rigid while operating with its maximum payload. Figure 14 shows values of HIC_{36} and peak contact force for different robot payloads and different linkage spring preloads in impact simulations including a lumped mass equal to the payload values depicted. The simulations discussed next concern a robot arm of 6 kg mass, 20 mm cover thickness, proximal link length, $L_1 = 0.6 \cdot L$ and impact velocity of 2 m/s. As expected, the linkage's contribution to safety decreases as the mass at the end effector increases, such that, for very high payloads, the effects of the linkage become negligible. In Figure 14, for the sake of simplicity, it has been assumed a constant robot arm mass regardless of the payload, with payloads ranging from 0 kg to 4 kg. As previously shown in Figure 11, peak contact force reduction decreases with linkage initial compression, and similar results are obtained for the reduction on HIC_{36} values. Regarding the applicability of the linkage, it must be noted that an initial compression (x_{so}) of 10 mm is enough to keep the linkage undeformed when a static or quasi-static load of 40 N is applied at the end effector, which still significantly contributes to safety. Normally, the initial compression of the linkage might be larger than this value and would need to be calculated taking into account the inertial forces in addition to gravity loads.

Robot speed is one of the most important factors regarding the impact severity, thus it should be limited to a maximum value which will depends on the mass carried at the end effector of the robot. Figure 15 represents HIC_{36} values for different robot payloads at different impact velocity. The simulation results show that for the particular set of mechanical parameters describing the simulated, its speed should be limited to ~ 1.80 m/s to guarantee a HIC_{36} value below 10, assumed as the human head safety limit, when carrying a payload of 2 kg. This speed limit can be improved by increasing the thickness

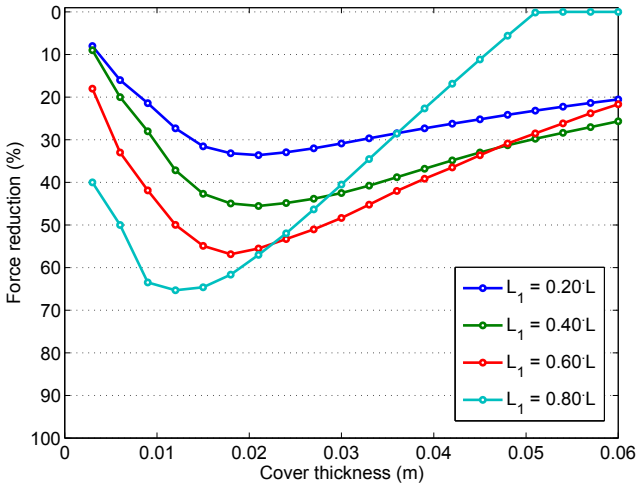

Figure 12: Peak contact force reduction (with respect to the rigid link) vs. cover thickness for different location of the linkage (equal robot arm length, L=0.7 m). Linkage initial compression x_{so}=20 mm.

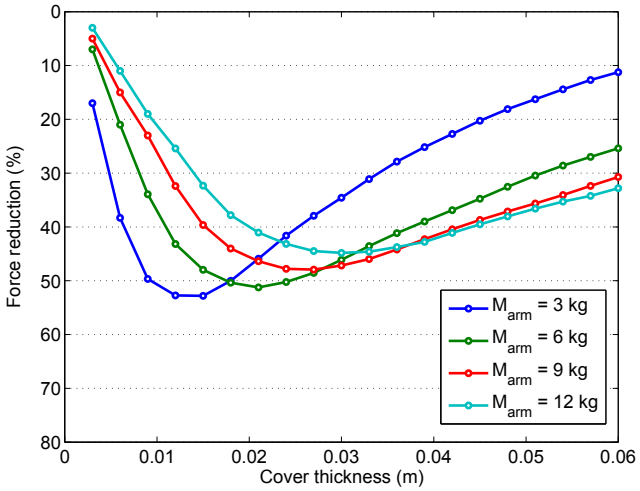

Figure 13: Peak contact force reduction (with respect to the rigid link) vs. cover thickness for different robot arm mass. Linkage initial compression x_{so}=20 mm and $L_1 = L_2$.

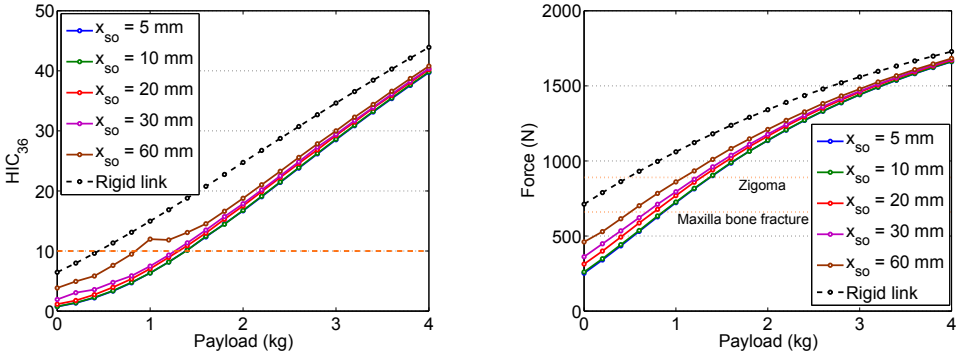

(a) (b)

Figure 14: HIC_{36} (a) and peak contact force (b) vs. payload for different linkage initial compression x_{so}. Simulated for a 6 kg robot arm mass, 20 mm cover thickness and proximal link length $L_1 = 0.6 \cdot L$.

of the robot cover. Figure 16 shows HIC_{36} values for different robot payload and cover thicknesses for a constant impact speed of 2 m/s. From the results, it becomes clear that larger payloads become admissible with thicker covers.

Up to this point we have only discussed the effects of a certain linkage design parameter, namely the initial compression of the linkage spring, i.e. the torque threshold, since it is the most relevant single parameter affecting the behavior of the linkage under an impact. However, it is also worth studying the influence in the impact response of the linkage stiffness value, once the torque threshold T_i is surpassed. This stiffness value is given by Eq. (6), and depends on the spring stiffness constant (K_s) and the rotation radius (r) of the linkage (Figure 3). Then, assuming the same torque threshold, different spring stiffness and rotation radius combinations will have effects in the HIC_{36} values. The results depicted in Figure 17 reveal a minor influence of the spring stiffness, K_s, on the impact severity, with a maximum increment of 4 % in the HIC_{36} for springs with stiffness between 5 kN/m and 160 kN/m. Similar results are found for changes in the rotation radius r, with the limitation that this distance is constrained to a narrow range of values due to mechanical design considerations.

4. Experimental results

4.1. Mechanical implementation

Figure 18 shows the flexible linkage prototype built with the purpose of experimentally validate the theoretical behavior derived in the previous section. The two base parts of the linkage face to each other with 12 steel spheres laying between them on a circular array at a distance of 28 mm from the linkage longitudinal axis. The choice of spheres has been done by considering that they should allow the linkage rotation around any rotation axis direction and simultaneously preventing linkage torsion rotation in the undeformed and small-deformation configurations. The flexible element of this linkage is a compression spring with an stiffness constant of $K_s = 44.0$ kN/m and a length at rest of 76 mm. Cable preload is achieved by a tensor, placed at a cap on the free end of the spring. The other end of the cable is firmly fixed to the other base part.

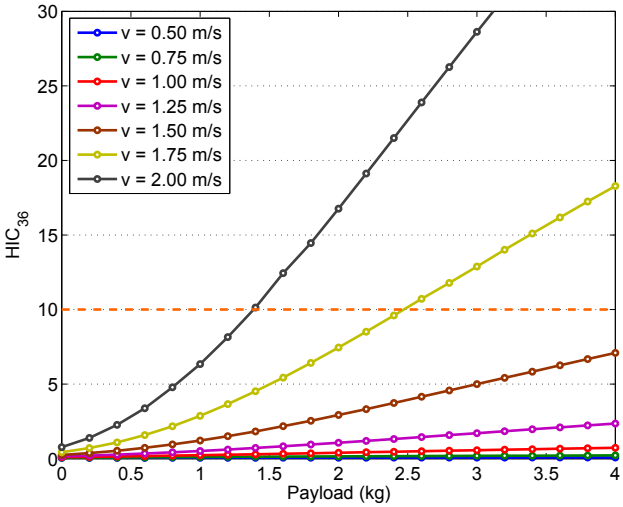

Figure 15: HIC_{36} vs. payload for different impact velocities. Simulated for a 6 kg robot arm mass, 20 mm cover thickness, x_{so}= 10 mm and proximal link length $L_1 = 0.6 \cdot L$.

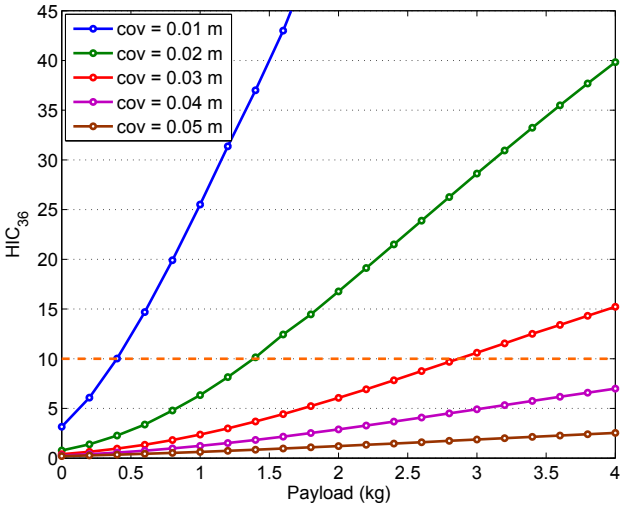

Figure 16: HIC_{36} vs. payload for different cover thickness. Simulated for a 6 kg robot arm mass, 2 m/s impact velocity, x_{so}= 10 mm and proximal link length $L_1 = 0.6 \cdot L$.

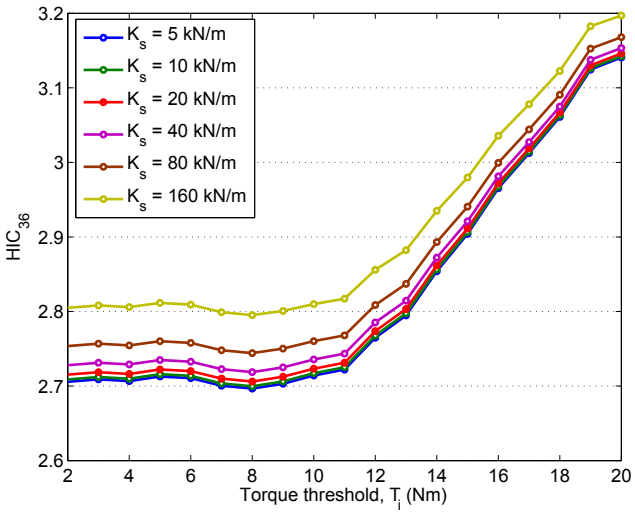

Figure 17: HIC_{36} vs. torque threshold for different linkage spring stiffness constant. Simulated for a 6 kg robot arm mass, 2 m/s impact velocity, 20 mm cover thickness, x_{so}= 10 mm and proximal link length $L_1 = 0.6 \cdot L$.

4.2. Characterization

Next we provide an experimental validation of the theoretical prediction of the mechanism stiffness. The expected behavior of the proposed flexible linkage, based on Eqs. (5)–(6), was graphically represented in Figure 5.

In order to validate these predictions, we have characterized the linkage prototype using the experimental setup depicted in Figure 19, where a torque is transmitted to the proximal link shaft through a force applied at a constant moment arm of 15 cm. The force level was increased by adding different masses to a wired-suspended container. Further

Figure 18: The flexible linkage prototype. The two rigid links have been removed here to better expose the mechanism, normally hidden inside the hollow links.

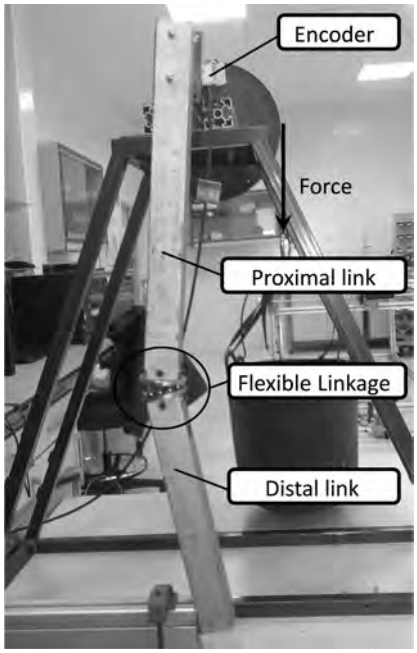

Figure 19: Experimental setup for characterizing the mechanism stiffness.

details on the description of the testbed are given in next section. The calculated torque curve at flexible linkage for different spring preload values are presented in Figure 20 together with the theoretical predictions.

All obtained curves initially show a high stiffness for the undeformed configuration of the linkage, then abruptly falling to a fairly constant stiffness when the linkage start rotating. The first segment of high stiffness corresponds to the structural flexibility of the elements that built up the experimental workbench while the linkage itself does not experience a real rotation (please, note that the encoder is located at the shaft of rotation of the arm, and the rotation angle (β) of the linkage is derived from the lengths of proximal and distal links and from the measured angle of the encoder). The slope of the second segment of the curves is dominated by the flexibility of the proposed linkage, much smaller than the aforementioned structural stiffness. Together with the experimental torque curves Figure 20 shows the predictions from the mathematical model derived above, which remarkably approximates the real behavior. One can also determine the torque thresholds from these curves, which also agree with the theoretical predictions as summarized in Table 4. Note that the results shown in Table 4 correspond to a single test and, therefore, do not include any statistical treatment.

To conclude the discussion of this experimental characterization, it can be confirmed that the arm with flexible linkage remains behaving as a rigid arm as long as the load torque does not surpass the established threshold, which during normal usage should be set slightly above the nominal robot operation load. Thus, the robot arm will operate as a common rigid-links arm unless a static or dynamic overload occurs, e.g. a misplacement of the end effector or an unexpected impact.

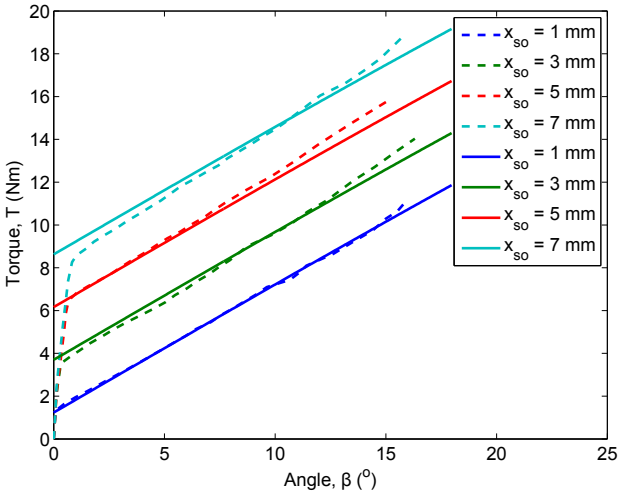

Figure 20: Theoretical (solid lines) and experimental (dashed) torque curves for the flexible linkage prototype, for different initial compresion (x_{so}) values.

Table 4: Observed and theoretical comparison of stiffness and threshold values.

Initial compression (x_{so})	Stiffness (Nm/rad)		Torque threshold (Nm)	
	Observed	Theoretical	Observed	Theoretical
1mm	37.1	34.5	1.32	1.23
3 mm	39.6	34.5	3.53	3.70
5 mm	39.3	34.5	6.30	6.16
7 mm	39.2	34.5	8.26	8.62

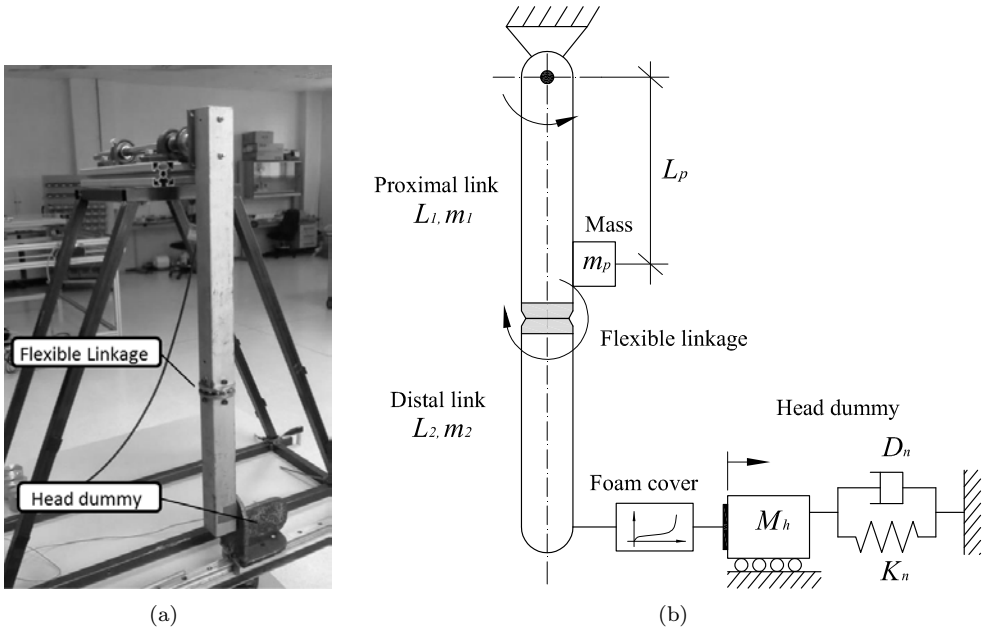

(a) (b)

Figure 21: Testbed with pendulum with flexible linkage and dummy (a). Simplified impact model of the testbed (b).

4.3. Experimental setup and results of impact tests

With the aim of experimentally confirm the contribution of the flexible linkage on impact force and head acceleration reduction, various experiments has been carried out in an impact testbed. The testbed developed consists of a pendulum mechanism, which link incorporates the flexible linkage, and a head dummy (Figure 21(a)). Pendulum link is then divided into proximal and distal links. Also, different additional lumped masses have been fixed to the proximal link to study the influence of changes in the relationship between masses of both links. The translational 1 d.o.f dummy is a sliding mass joined with a spring to the base [2]. The physical parameters of pendulum and head dummy depicted in Figure 21(b) are summarized in Table 5. In the contact area, two different cover materials has been used, the 12 mm polyurethane specimen characterized in Section 3, and a stiffer 2 mm thickness rubber.

The testbed was instrumented with a piezoelectric accelerometer ICP-356A15 located at the translational dummy to measure the acceleration of the head, with a measurement range of ±500 g and 2 Hz to 5 kHz frequency range. The different tests were carried out by dropping the pendulum link from a certain angle (relative to the vertical) and recording the signals with a data acquisition system.

Several impact tests have been carried out with different additional mass (m_p) and the two kinds of covers. The pendulum is released from a 26º angle, with an approximated impact velocity of 1.4 m/s (impact speed will vary depending on the value of m_p). Same tests have been repeated for different torque threshold of the linkage, i.e. different initial compression, x_{so}, and for the linkage physically locked by four internal bolts. Figure 22 shows the measured acceleration of the dummy with no additional mass and for 0.9

Table 5: Parameters of the impact testbed.

Property	Value
Mass (kg)	$m_1 = 1.25, m_2 = 0.75, M_h = 3.25, m_p = [0, 0.9, 2.7]$
Length (m)	$L_1 = 0.46, L_2 = 0.26, L_p = 0.41$
Stiffness (N/m)	$K_n = 460$
Damping (Ns/m)	$D_n = 11.6$

kg and 2.7 kg additional mass when polyurethane foam is used, which clearly shown the reduction on the first impact peak (39 %, 45 % and 55 %, respectively) when the rotation of the linkage is allowed.Note that previous percentages are obtained from a single experiment and therefore do not include any statistical treatment. As expected, larger mass of the proximal link results in higher head acceleration reduction. Initial compressions have been changed from 1 mm to 7 mm, the larger compressions show small increments in the first peak acceleration and noticeable time advance of the second peak. All this experimental results are in accordance with those obtained in simulations of Section 3. Regarding the applicability of the linkage, the initial compression used of 7 mm corresponds to a torque threshold of 8.3 Nm. This value means that, e.g. a robot arm incorporating the flexible linkage placed at 20 cm from the end effector, allows a static payload of 41 N without deformation of the linkage, improving safety conditions at the same time. This configuration is suitable, for example, for a service robot working in domestic environments, where a typical payload is smaller than 20 N.

Finally, impact tests have been repeated for the 2 mm rubber cover. Similarly to the simulation results for rigid impacts (Figure 10), first acceleration peak remain almost constant regardless the linkage where locked or not (Figure 23). In other way, some differences appear after the first impact. Several impacts or rebounds of relative high values are shown when the linkage is locked, which may produce greater injury compared to the unlocked linkage configuration, where lower second impacts are present.

5. Conclusions

A new safety system to be included in robot arms that work in collaborative scenarios has been presented in this paper. The safety system consists of a compliant linkage that can be located within the length of the links of a robot arm. By inserting the flexible linkage in a robot arm link, the link is in fact divided in two segments connected by this special joint. The most relevant feature of the flexible linkage is its ability to decouple the inertia at each side of it in an impact situation. The flexible linkage allows the relative rotation of one segment with respect to the other. The proposed linkage has a torque threshold under which the relative rotation does not take place and the two segments remain aligned. As explained in the paper the torque threshold can be mechanically adjusted by modifying the preload of a spring. Simulation has been used to investigate the contribution of the proposed linkage to the reduction of contact force and induced acceleration in the case of an impact between the end effector of a robot arm and a human head. The relation of the contact force reduction, the cover thickness and the initial compression of the linkage has been studied by means of several simulations, showing that for any initial compression there exists a cover thickness value where the

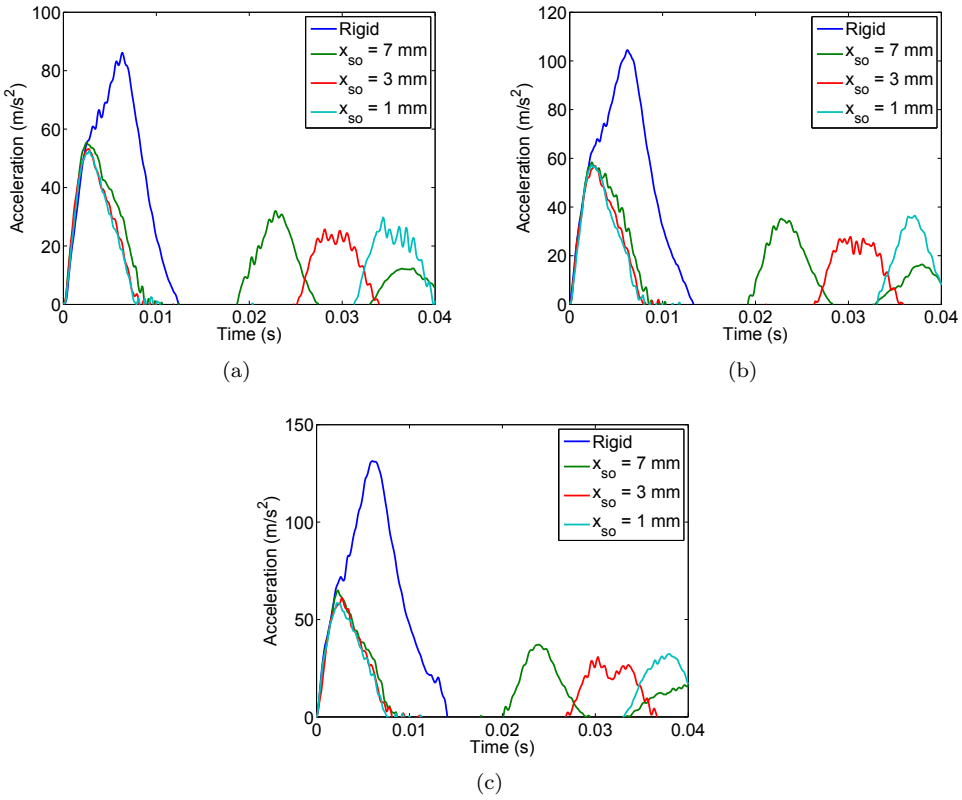

Figure 22: Dummy acceleration for different linkage preloads and polyurethane cover: with no additional mass, $m_p = 0$ kg (a), with additional mass, $m_p = 0.9$ kg (b), and with $m_p = 2.7$ kg (c).

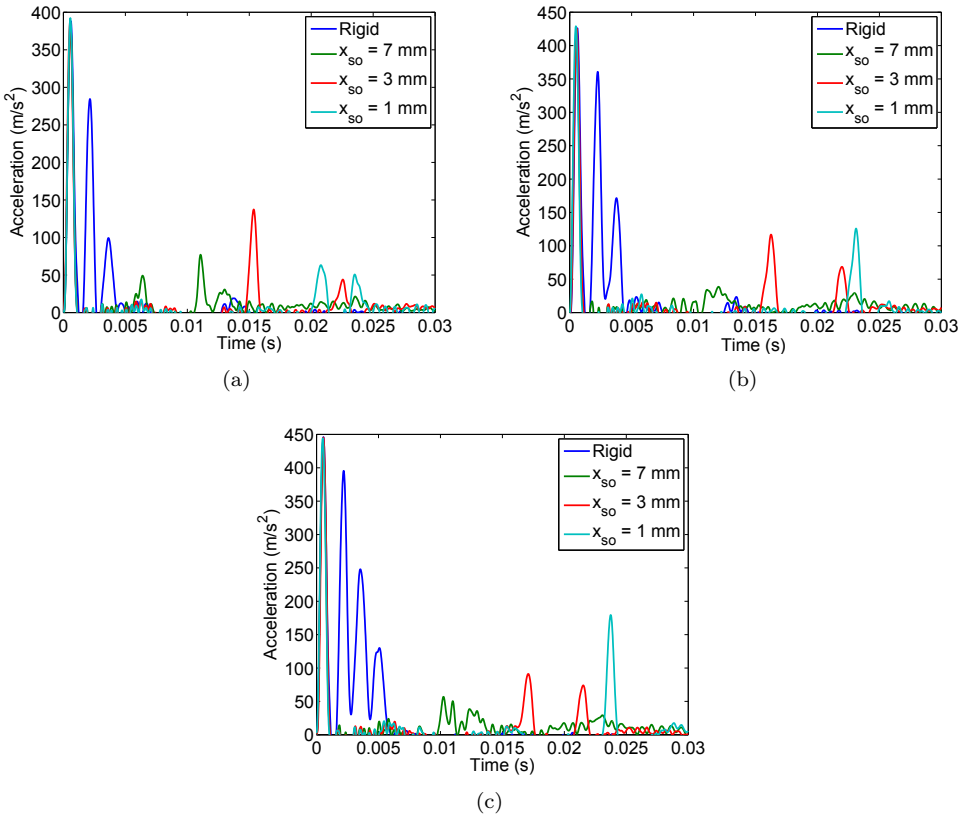

Figure 23: Dummy acceleration for different linkage preloads and rubber cover: with no additional mass, $m_p = 0$ kg (a), with additional mass, $m_p = 0.9$ kg (b), and with $m_p = 2.7$ kg (c).

force reduction due to the linkage is maximized. Peak contact force reductions over 50% have been predicted in several simulated scenarios. A test bed has been used to study the performance of a link including the proposed flexible linkage, showing that the acceleration of the dummy head is significantly reduced. The proposed linkage has therefore shown a promising ability of increasing safety in impact situations.

Acknowledgements

This work has been partially funded by the Spanish "Ministerio de Ciencia e Innovación" under the project "DAVARBOT" (DPI 2011-22513) and the grant program JDC-MICINN 2011.

Bibliography

[1] A. De Santis, B. Siciliano, A. De Luca, A. Bicchi, An atlas of physical human–robot interaction, Mechanism and Machine Theory 43 (3) (2008) 253–270.

[2] J. López-Martínez, D. García-Vallejo, A. Giménez-Fernández, J. Torres-Moreno, A flexible multibody model of a safety robot arm for experimental validation and analysis of design parameters, Journal of Computational and Nonlinear Dynamics 9 (1) (2014) 011003.1–011003.10.

[3] R. Ham, T. Sugar, B. Vanderborght, K. Hollander, D. Lefeber, Compliant actuator designs, Robotics Automation Magazine, IEEE 16 (3) (2009) 81–94.

[4] H.-S. Kim, J.-J. Park, J.-B. Song, Safe joint mechanism using double slider mechanism and spring for humanoid robot arm, in: IEEE-RAS International Conference on Humanoid Robots, IEEE, 2008, pp. 73–78.

[5] S.-S. Yoon, S. Kang, S.-K. Yun, S.-J. Kim, Y.-H. Kim, M. Kim, Safe arm design with mr-based passive compliant joints and visco-elastic covering for service robot applications, Journal of mechanical science and technology 19 (10) (2005) 1835–1845.

[6] T. Sugaiwa, H. Iwata, S. Sugano, Shock absorbing skin design for human-symbiotic robot at the worst case collision, in: IEEE-RAS International Conference on Humanoid Robots, IEEE, 2008, pp. 481–486.

[7] L. Zeng, G. Bone, Design of elastomeric foam-covered robotic manipulators to enhance human safety, Mechanism and Machine Theory 60 (1) (2013) 1–27.

[8] D. Hyun, H. Yang, J. Park, Y. Shim, Variable stiffness mechanism for human-friendly robots, Mechanism and Machine Theory 45 (6) (2010) 880–897.

[9] J. López-Martínez, J. Blanco-Claraco, D. García-Vallejo, J. Torres-Moreno, A. Giménez-Fernández, Avastt: A new variable stiffness actuator with torque threshold, in: ROBOT2013: First Iberian Robotics Conference, Vol. 252 of Advances in Intelligent Systems and Computing, 2014, pp. 573–583.

[10] S. Haddadin, A. Albu-Schäffer, O. Eiberger, G. Hirzinger, New insights concerning intrinsic joint elasticity for safety, in: IEEE/RSJ International Conference on Intelligent Robots and Systems, IEEE, 2010, pp. 2181–2187.

[11] S. Dwivedy, P. Eberhard, Dynamic analysis of flexible manipulators, a literature review, Mechanism and Machine Theory 41 (7) (2006) 749–777.

[12] J.-J. Park, H.-S. Kim, J.-B. Song, Safe robot arm with safe joint mechanism using nonlinear spring system for collision safety, in: IEEE International Conference on Robotics and Automation, IEEE, 2009, pp. 3371–3376.

[13] J.-J. Park, B.-S. Kim, J.-B. Song, H.-S. Kim, Safe link mechanism based on nonlinear stiffness for collision safety, Mechanism and Machine Theory 43 (10) (2008) 1332–1348.

[14] N. Mills, A. Gilchrist, The effectiveness of foams in bicycle and motorcycle helmets, Accident Analysis and Prevention 23 (2–3) (1991) 153–163.

[15] M. Simoneau, M. Denninger, T. Hain, Role of loading on head stability and effective neck stiffness and viscosity, Journal of Biomechanics 41 (2008) 2097–2103.

[16] M. Fard, T. Ishihara, H. Inooka, Identification of the head-neck complex in response to trunk horizontal vibration, Biological Cybernetics 90 (6) (2004) 418–426.

[17] J. Tangorra, L. Joones, I. Hunter, Dynamics of the human head-neck system in the horizontal plane, Annals of Biomedical Engineering 31 (5) (2003) 606–620.
[18] L. Gibson, M. Ashby, Cellular solids: structure and properties, 2nd Edition, Cambridge solid state science series, Cambridge University Press, 1997.
[19] K. Rusch, Load-compression behavior of flexible foams, Journal of Applied Polymer Science 13 (11) (1969) 2297–2311.
[20] M. Avalle, G. Belingardi, A. Ibba, Mechanical models of cellular solids: Parameters identification from experimental tests, International Journal of Impact Engineering 34 (1) (2007) 3–27.
[21] J. Versace, A review of the severity index, in: SAE Technical Paper 710881, 1971.
[22] J. McKillop, C. Willis, A. Roberts, New methods for assessing facial injury risk. proyect report 237, in: Transport Research Foundation, 2007.
[23] A. Bicchi, G. Tonietti, Fast and 'soft-arm' tactics, IEEE Robotics and Automation Magazine 11 (2) (2004) 22–33.